Reciprocal space mapping of magnetic order in thick epitaxial MnSi films

B. Wiedemann,[1] G. L. Causer,[1] A. Chacon,[1] S. L. Zhang,[2] Y. Khaydukov,[3,4] T. Hesjedal,[2,*] O. Soltwedel,[1,3,4] T. Keller,[3,4] S. Mühlbauer,[5] T. Adams,[1] M. Halder,[1] C. Pfleiderer,[1,5,6,7,†] and P. Böni[1]

[1]*Physik Department, Technische Universität München, James-Franck-Strasse 1, 85748 Garching, Germany*

[2]*Clarendon Laboratory, Department of Physics, University of Oxford, Parks Road, Oxford OX1 3PU, United Kingdom*

[3]*Max-Planck-Institut für Festkörperforschung, Heisenbergstrasse 1, 70569 Stuttgart, Germany*

[4]*Max Planck Society, Outstation at FRM-II, D-85748 Garching, Germany*

[5]*Forschungsneutronenquelle Heinz Maier Leibnitz (FRM II), Technische Universität München, 85748 Garching, Germany*

[6]*Munich Center for Quantum Science and Technology (MCQST), D-85748 Munich, Germany*

[7]*TUM Center for QuantumEngineering (ZQE), Technical University of Munich, D-85748 Garching, Germany*

(Received 2 October 2017; revised 17 August 2026; accepted 30 September 2026; published 2 November 2026)

We report near-surface small-angle neutron scattering (NS-SANS) and complementary off-specular neutron reflectometry (OSR) of the magnetic order in a single-crystalline epitaxial MnSi film grown on Si(111) in the thick-film limit. Providing a means of direct reciprocal space mapping, NS-SANS and OSR reveal one-dimensional magnetic modulations perpendicular to the film surface under magnetic fields parallel and perpendicular to the film surface, where additional polarized neutron reflectometry (PNR) and magnetization measurements are in excellent agreement with the literature. Regardless of the field orientation, our data do not suggest the presence of more complex spin textures, notably the formation of skyrmions. This observation establishes a distinct contrast to bulk MnSi thinned to similar nanoscale thicknesses, in which a skyrmion lattice dominates the phase diagram under perpendicular fields. Extended x-ray absorption fine structure measurements suggest that small shifts of the Si positions within the unstrained unit cell of the film control the magnetic state, representing the main structural difference between epitaxial and thinned bulk MnSi.

DOI: 10.1103/pss4-vlyr

I. INTRODUCTION

The discovery of skyrmions in chiral magnets [1–13] has generated a flurry of efforts to exploit their unusual properties technologically [14–19]. Initially identified in a small pocket of the phase diagram of the cubic chiral magnets MnSi, $Fe_{1-x}Co_xSi$, FeGe, and Cu_2OSeO_3, Lorentz transmission electron microscopy (LTEM) early on revealed a strong increase of the extent of the skyrmion phase in bulk samples thinned to reduced thicknesses [5–7,20,21]. While this observation demonstrated that nanoscaled systems may be ideally suited to host skyrmions, nonconformity between the phase diagrams of thinned bulk samples and epitaxial films of comparable thickness prepared by established deposition techniques has meant that the mechanisms controlling the magnetic properties of epitaxial B20 films have remained unresolved.

Based on measurements of the magnetization and magneto-transport, interpreted to provide a topological Hall signal for magnetic fields applied perpendicular to the film surface, seminal work on epitaxial MnSi [22–26], $Mn_{1-x}Fe_xSi$ [27], $Fe_{1-x}Co_xSi$ [28,29], and FeGe [30–32], as well as more recently epitaxial oxide bilayers [33], claimed the formation of skyrmions. However, the phase diagrams reported for nominally the same film thickness differed between different studies, as well as from those determined by means of LTEM on thinned bulk samples because the removal of the substrate in free-standing films changes the elastic properties of the film [32]. Interpretation of LTEM contrasts in epitaxial MnSi/Si(111) remains under active discussion. While Monchesky *et al.* attribute similar patterns to moiré fringes that can persist in focus and can be removed by small tilts, Li *et al.* present focus-dependent contrasts consistent with magnetic origin [34,35]. This discrepancy is not yet resolved. Importantly, alternative mechanisms have been proposed explaining the LTEM data without invoking skyrmions or topological textures [34,36].

Similar uncertainties exist under magnetic fields applied parallel to the film surface. Here, magnetization and magnetotransport have been interpreted to provide putative evidence of complex magnetic phase diagrams supporting the formation of in-plane skyrmions [23,37–40]. However, subsequent microscopic measurements using polarized neutron reflectometry (PNR) [41–43], while suggesting modulations

*Contact author: thorsten.hesjedal@physics.ox.ac.uk

†Corresponding author: christian.pfleiderer@ph.tum.de

Published by the American Physical Society under the terms of the Creative Commons Attribution 4.0 International license. Further distribution of this work must maintain attribution to the author(s) and the published article's title, journal citation, and DOI.

perpendicular to the film surface, failed to resolve the situation convincingly, as the technique requires the assumption of complex scattering profiles where the uniqueness of a solution is not always guaranteed. Additionally, PNR averages across the sample plane [44], complicating the analysis of in-plane modulated magnetic structures, such as in-plane skyrmions.

Theoretically, it was at first believed that the increased extent of the skyrmion phase in thinned bulk samples originated from the destabilization of the competing magnetic phases [5,6,45]. Recent studies suggest instead that free surfaces favor the formation of skyrmions energetically, driving the formation of skyrmions in surface-dominated systems [43,46–48]. Further considerations include interface-induced spin–orbit coupling effects, which are dominant for heavy element substrates as used in studies of atomically thin films of Fe and FePd [49,50]. Last but not least, numerous studies have considered magnetic anisotropies induced by the lattice mismatch with the substrate [23,42,51–54], which, however, are found to decrease rapidly with increasing film thickness.

In view of these complexities an important point of reference is the lack of correspondence between the phase diagrams of thinned bulk B20 compounds, providing a well-defined setting, and epitaxial layers of comparable thickness. For epitaxial FeGe on Si(111), where the lattice mismatch is vanishingly small, there is compelling microscopic evidence that, for fields applied parallel to the film surface, the magnetic order consists of helical modulations perpendicular to the film surface without any evidence for more complex textures, notably skyrmions [55]. The pronounced differences between the magnetic order in epitaxial films and thinned bulk samples appear to be well beyond present understanding, establishing that dimensionality and global strain cannot be the main drivers of the phase diagrams alone, and underscoring the need for further unbiased microscopic investigations to reveal the inherent structural and magnetic differences.

To establish the nature of the long-range magnetic order in epitaxial B20 films unambiguously, direct reciprocal space imaging by means of neutron scattering is ideally suited. Meaningful diffraction patterns are already expected for the short correlation lengths akin to the regime of small-angle neutron scattering (SANS). Comparisons of the calculated SANS patterns arising from the magnetic structures typically considered in epitaxial films of B20 compounds can be found in the Supplemental Material (SM) [56] (see also Refs. [57–61] therein). A major technical constraint of performing conventional SANS on nanoscale films is, however, the minuscule scattering volume of the sample. For instance, a SANS study on a 267 Å-thick MnSi film demonstrated that even for a measurement time of 20 hours the magnetic signal was barely discernible [40]. In comparison, positioning the neutron beam at a shallow angle of incidence to the film surface just above the critical angle of reflection, the near-surface (NS) SANS configuration is reached [62,63], where a clear scattering signal was demonstrated on a stack of 32 FeGe films ($15 \times 15\,\mathrm{mm}^2$ corresponding to 12 mg of material) [55]. Unfortunately, that work required the preparation of several identical and perfectly aligned films, bearing the additional risk that important details may get averaged out, hindering analysis. In contrast, the NS-SANS measurements presented here are performed on a single film above the critical angle of total external reflection, providing sufficient intensity and surface sensitivity to resolve nanoscale modulations along Q_z and, if present, also along Q_x and Q_y [63]. To achieve this, we apply magnetic fields both parallel and perpendicular to the scattering direction, allowing the spin texture to be imaged in every possible orientation with respect to the neutron beam.

II. EXPERIMENTAL METHODS

In our study, reciprocal space mapping was used as a direct, microscopic probe of the internal magnetic order of epitaxial B20 films. We demonstrate that NS-SANS and off-specular neutron reflectometry (OSR) can be performed on just a single film rather than a multifilm stack, allowing clear and unambiguous analysis [64]. In our experiments, NS-SANS is sensitive to nanoscale correlations in Q_x, Q_y, and Q_z, while OSR and PNR are sensitive to nanoscale correlations in Q_z. Additionally, OSR is sensitive to microscale correlations in Q_x (see Sec. II of the SM [56]). Thus, through the combination of NS-SANS, PNR, and OSR, full phase-space determination with nanoscale resolution in Q_x, Q_y, and Q_z is achieved to provide a complete set of experimental data on a single film. We focus on the properties of epitaxial MnSi on Si(111) as it allows for comparisons with well-defined thinned bulk MnSi, as well as the large body of literature on thinned bulk and epitaxial FeGe. We find one-dimensional magnetic modulations perpendicular to the MnSi film surface featuring magnetic phase diagrams under parallel and perpendicular field that are highly reminiscent of those identified in epitaxial FeGe [55]. Moreover, extended x-ray absorption fine structure (EXAFS) on the epitaxial MnSi film reported elsewhere [65] reveals that the lattice mismatch with the substrate is released within a few atomic layers. As a result, the film displays unstrained lattice parameters but with small shifts of the Si positions normal to the film plane. Our results, taken together with the work on epitaxial FeGe, suggest the formation of one-dimensional magnetic modulations perpendicular to the film surface as a common trend observed in both MnSi and FeGe films of similar thickness, most likely because of tiny shifts of the nonmagnetic atoms in otherwise unstrained film lattices.

Epitaxial MnSi(111) films were grown on Si(111) substrates by molecular beam epitaxy using a two-step growth procedure (see the SM [56] for details). First, approximately three monolayers of Mn were deposited on Si(111)-(7×7) at room temperature and subsequently annealed at 400 °C. This process formed an epitaxial MnSi seed layer via reactive solid-phase epitaxy, following the method described in Ref. [22]. Second, the MnSi film was grown to the desired thickness by simultaneous codeposition of Mn and Si under stoichiometric flux conditions at substrate temperatures of 250–300 °C. Under these conditions, the B20 phase forms directly during growth. Optionally, a post-growth anneal was performed at 400 °C to improve film quality.

For this work, we studied three MnSi films with thicknesses $d = (390 \pm 10)$ Å, (495 ± 10) Å, and (553 ± 10) Å. Each film is thicker than the wavelength of the magnetic helix of ∼180 Å in bulk MnSi and is in the thick-film limit well above the thickness of ∼120 Å, where T_c has been reported to become thickness independent [22]. All samples displayed the same structural and magnetic properties, apart

from small differences of the magnetic modulation length of order 10 %, as presented in the SM [56]. Moreover, the induced uniaxial anisotropy is vanishingly small [37,66]. The electrical resistivity of the 553 Å film yields a temperature dependence and residual resistivity $\rho_0 \approx 23\,\mu\Omega\,\mathrm{cm}$ consistent with the literature (see Sec. IV D of the SM [56] for a detailed discussion). The kink observed near 45 K corresponds with the magnetic ordering temperature reported previously for thick epitaxial MnSi films. The MnSi film with a thickness of 553 Å displayed structural and magnetic properties in excellent agreement with data reported in the literature [22–24,37,38,41–43,67–69], and was subsequently chosen for the neutron scattering investigations.

For the neutron experiments, this film was capped with a 310 Å Cu layer to enhance the neutron cross-section and to protect against surface oxidation (see Sec. IV A and Fig. S3 within the SM [56]). Grazing-incidence x-ray diffraction (GIXRD; Cu Kα) was measured with the sample azimuth offset from strong Si and MnSi reflections to screen for secondary phases. The neutron sample shows no additional peaks in GIXRD (see Sec. IV A, Fig. S5 within the SM [56]). The in-plane epitaxy is established by ϕ scans of Si(422) and MnSi(211) (see Fig. S4 within the SM [56]).

III. EXPERIMENTAL RESULTS

Figure 1(a) shows the NS-SANS setup used in our study. Measurements were carried out at SANS-1 at the Heinz Maier-Leibnitz Zentrum (MLZ), Munich [70]. NS-SANS data were recorded for fields parallel and perpendicular (see Sec. V A of the SM [56]) to the surface of the MnSi film. The sample was illuminated at an incident angle of $\theta_i = 0.65°$, being above the critical angle of reflection of MnSi ($\theta_c = 0.076°$), using neutrons of wavelength $\lambda = (5.5 \pm 0.5)$ Å collimated over 8 m and recorded with a detector 6 m behind the sample. The choice of θ_i allowed for a good separation between the specular reflection (yellow arrow) and the magnetic Bragg peaks (A, B). Because of the magnetic mosaicity of the sample and the small scattering angles, Bragg peaks for both $+\boldsymbol{k}_h$ and $-\boldsymbol{k}_h$ could be observed simultaneously.

Typical data at $T = 15$ K for the MnSi film are shown in Figs. 1(b)–1(e) for fields applied parallel to the film surface and the neutron beam [as depicted in Fig. 1(a)] after subtraction of the background determined at 60 K. The direct beam in the center of the images was partially masked (blue square) to prevent saturation of the detector, yet permitting data analysis very close to the direct beam. In zero field, magnetic scattering intensity, labeled A, is observed at $|Q_z| = 0.067$ Å^{-1} [Fig. 1(b)], characteristic of a one-dimensional magnetic modulation normal to the film surface propagating along the [111] sample axis. In view of the bulk properties of MnSi we assume the formation of helical modulations, where, as compared to bulk MnSi, the wavelength of the modulation in the film is a factor of two smaller, with a distribution of modulation lengths on the order of 20%. At 0.4 T, an additional magnetic scattering intensity, labeled B, is observed at $|Q_z| = 0.052$ Å^{-1} [Fig. 1(c)]. At 0.55 T, the scattering intensity of B persists in the absence of A [Fig. 1(d)], while at 0.8 T no magnetic scattering is detected from the MnSi film [Fig. 1(e)].

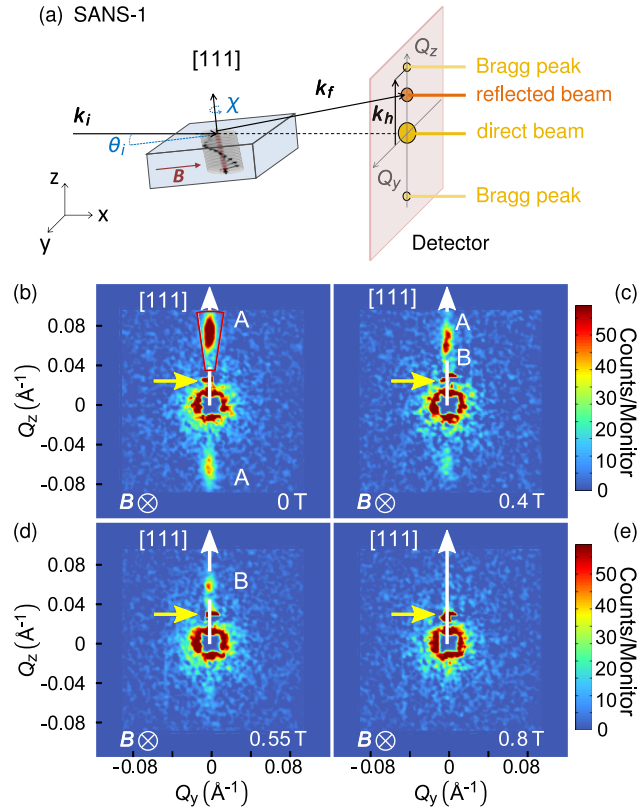


FIG. 1. Key aspects of the NS-SANS studies at SANS-1. (a) Schematic NS-SANS setup. The incident neutron beam illuminates the MnSi film at an incidence angle $\theta_i = 0.65°$. $\boldsymbol{B}$ was applied either parallel or perpendicular (see Sec. V A of the SM [56]) to the film surface. (b)–(e) Typical NS-SANS data for the MnSi film at $T = 15$ K under increasing magnetic fields aligned along the forward direction [cf. panel (a)]. The yellow arrow marks the specular reflected beam. Bragg peaks labeled A and B arise from magnetic modulations along Q_z corresponding to $k_h^A = 0.067$ Å^{-1} and $k_h^B = 0.052$ Å^{-1}, respectively.

Linear intensity cuts of the NS-SANS data along Q_z at $Q_y \approx 0$ Å^{-1} are shown in Fig. 2. These data confirm that with increasing magnetic field the scattering intensity of the k_h^A modulation (i.e., label A in Fig. 1) sharpens without changing its location at $|Q_z| = 0.067$ Å^{-1}, while the k_h^B modulation (i.e., label B in Fig. 1) emerges above $\sim 0.2T$ at $|Q_z| = 0.052$ Å^{-1} and sharpens with increasing field. The intensity of the k_h^A modulation vanishes above $\sim 0.5T$ while the intensity of the k_h^B modulation continues to sharpen even further, until it vanishes above $\sim 0.8T$.

The same field evolution was observed for fields applied in the plane of the film but perpendicular to the neutron beam (see Sec. V A and Fig. S10 within the SM [56]). In this geometry, the film's magnetic spin texture is imaged in a "side-on" orientation compared to the "front-on" orientation of the NS-SANS measurements presented in Fig. 1, as the spin texture follows the external field [63]. As a result, the combination of these NS-SANS measurements probes nanoscale correlations in Q_z and Q_y (front-on orientation) and Q_z and Q_x (side-on orientation). (We note and adhere to the general NS-SANS convention of presenting data with respect to the

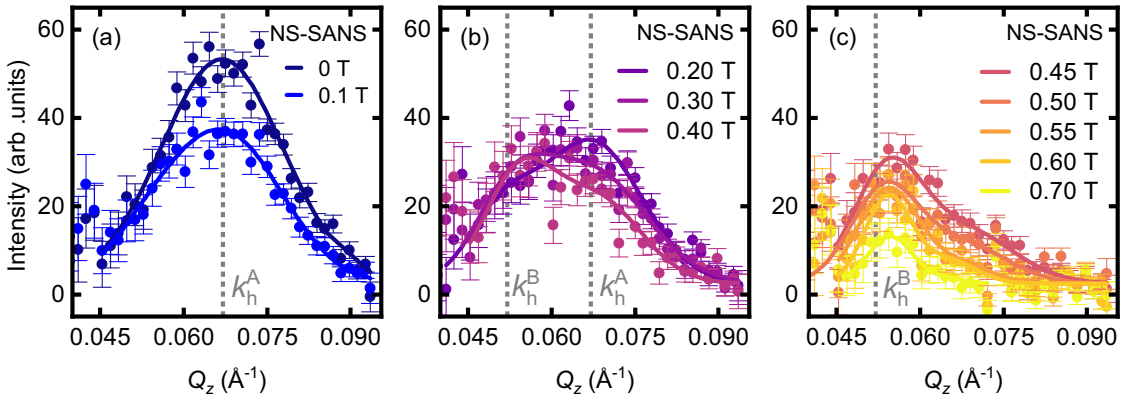


FIG. 2. Field-dependent NS-SANS line profiles. Intensity cuts along Q_z at $Q_y \approx 0\,\text{Å}^{-1}$ measured at 15 K for (a) regime 1, (b) the intermediate regime, and (c) regime 2. The peak at $k_h^A = 0.067\,\text{Å}^{-1}$ remains at fixed position, while a second peak at $k_h^B = 0.052\,\text{Å}^{-1}$ emerges above ∼0.2 T and sharpens with increasing field. For the designation of the regimes, see Figs. 5 and 6.

instrument frame of reference (i.e., not the sample frame of reference) and hence plot data as Q_z vs Q_y). Moreover, for fields applied perpendicular to the film surface, the NS-SANS data likewise show a magnetic modulation propagating along Q_z, albeit with a constant modulation length up to the onset of the field-polarized state at B_c (see Sec. V A and Fig. S9 within the SM [56]). Within the limits of the instrumental resolution, the NS-SANS data do not provide indications of scattering at finite Q_x or Q_y in the parameter regime explored (see Fig. S11 within the SM [56] for representative Q_y line profiles), suggesting that the nanoscale magnetic order in the film is purely one-dimensional along Q_z.

To complement the NS-SANS measurements, we performed PNR ($\theta_i = \theta_f$) and OSR ($\theta_i \neq \theta_f$) at the reflectometer NREX, MLZ [71]. While both PNR and OSR provide high-resolution information along Q_z, OSR additionally probes large lateral correlations along Q_x, which primarily describes the domain structure, rather than the nanoscale helical modulation, of the MnSi film. Measurements were performed using neutrons with a wavelength $\lambda = 4.31$ Å and a polarization parallel and antiparallel to the in-plane magnetic field $\boldsymbol{B}_y$ [Fig. 3(a)] to yield an improved Q_z resolution and corroborate the NS-SANS results.

Figures 3(b) and 3(c) show typical OSR data of the MnSi film at $T = 15$ K under an in-plane magnetic field $\boldsymbol{B}_x$ oriented along $[1\bar{1}0]$ (the x direction); the largest field accessible was 0.24 T. The vertical stripes (dark blue and red) for $Q_x = 0$ are owing to the specular reflection of the neutrons by the sample. The position of the Bragg sheets in Q_z, labeled A and B, provides information on the depth-dependent magnetic structure of the film and is sensitive to the helical modulations that span the film thickness. The Bragg sheets appear at $k_h^A = 0.067\,\text{Å}^{-1}$ and $k_h^B = 0.052\,\text{Å}^{-1}$, consistent with the helical wave vectors inferred from NS-SANS. The width of the Bragg sheets reflects the depth-averaged lateral correlation length of the film's magnetic domain structure. With increasing applied magnetic field, the Bragg sheets narrow, indicating an increase in the lateral correlation length of the film's magnetic domains. The weak intensity of the Bragg sheets is an indication of (i) the excellent quality of the samples and (ii) the excellent alignment of the helices perpendicular to the film even in large fields perpendicular to $\boldsymbol{k}_h$.

We now turn to the specular PNR results. Shown in Figs. 4(a1) and 4(b1) are the specular reflectivity R^{++} and R^{--} of polarized neutrons at $T = 35$ K for the MnSi film. Here, the field is applied along the y direction (parallel to $[11\bar{2}]$) and perpendicular to the incident neutron beam [Fig. 3(a)]. In Figs. 4(a2) and 4(b2), the corresponding spin asymmetries, defined as $(R^{++} - R^{--})/(R^{++} + R^{--})$, are displayed, together with best-fit calculations. The modeling of the PNR reflectivities is illustrated in Fig. 4(a3) and 4(b3) where the depth-dependent magnetization profiles extracted from the fits are shown. Data at low fields ($B_y = 0.03$ T) may be well accounted for by assuming a magnetic helix with a wave vector $k_h^A = 0.067\,\text{Å}^{-1}$ parallel to Q_z. This result compares with typical PNR at larger fields ($B_y = 0.44$ T) shown in Fig. 4(b1), where the reflectivity may be fitted by assuming an anharmonic helix with a smaller wave vector $k_h^B = 0.052\,\text{Å}^{-1}$ and the magnetic moments pointing predominantly along

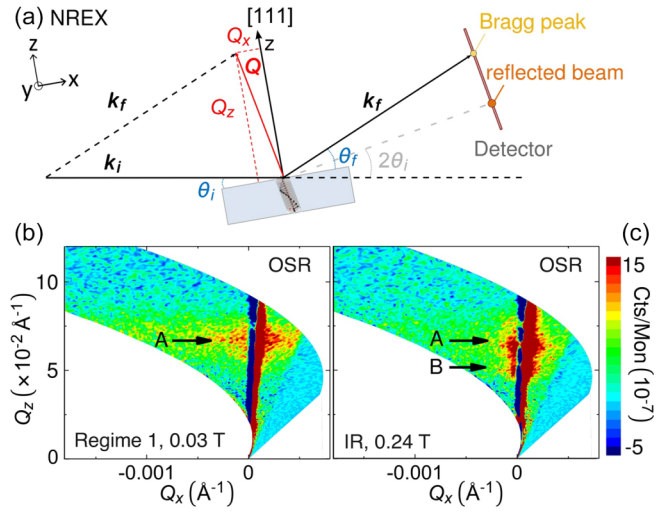


FIG. 3. Summary of key OSR data collected on the MnSi film using the reflectometer NREX. (a) Schematic of the OSR (and PNR) setup. The x direction is parallel to the $[1\bar{1}0]$ crystallographic direction, the y direction is parallel to $[11\bar{2}]$, and the z direction is taken as the epitaxial growth axis parallel to [111]. (b), (c) OSR recorded at $T = 15$ K for $B_x = 0.03$ T and $B_x = 0.24$ T, where a single modulation and two modulations are seen, respectively.

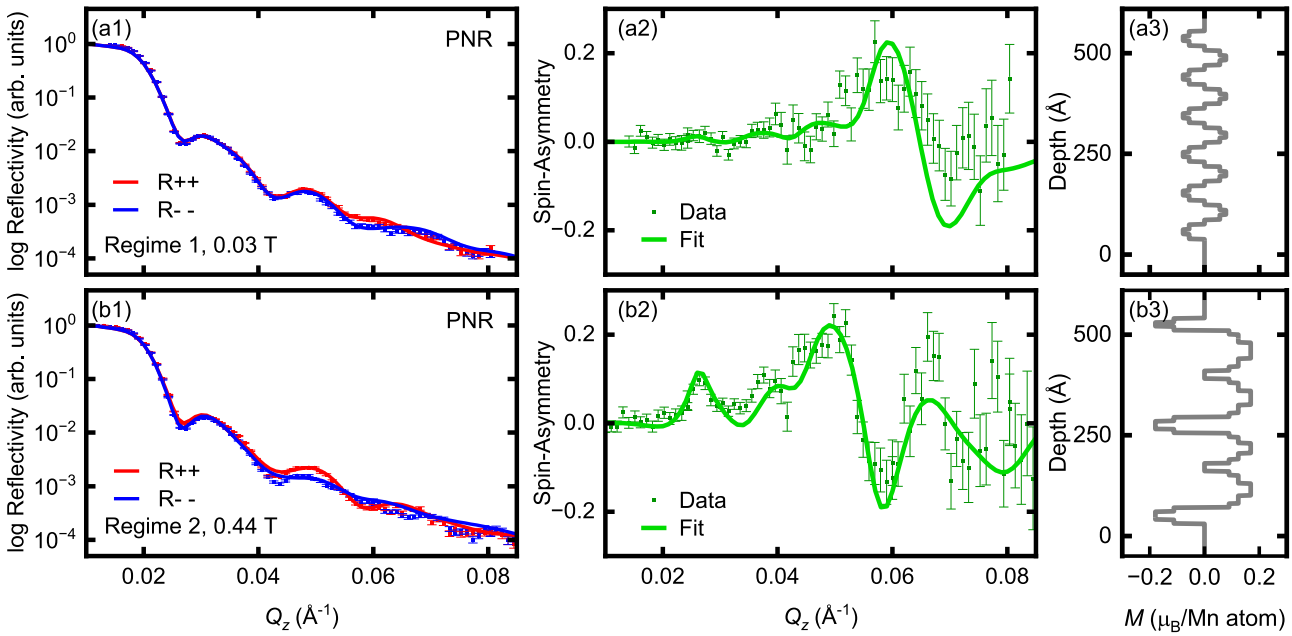


FIG. 4. PNR data and their analysis at 35 K. (a1), (b1) Specular reflectivities R^{++} and R^{--} recorded for $B_y = 0.03$ T (regime 1) and $B_y = 0.44$ T (regime 2), respectively, including best-fit model curves (solid lines). (a2), (b2) Spin asymmetries of the PNR data shown in (a1) and (b1) as a function of momentum transfer together with the model fits. (a3), (b3) Depth-dependent magnetization profiles $M(z)$ obtained from the best fits, showing a modulation predominantly along Q_z. Error bars are statistical.

$+\boldsymbol{B}_y$. The appearance of helices propagating parallel to Q_z inferred from our PNR data is in excellent agreement with our NS-SANS results, as well as with literature [38,41].

The field evolution of the Bragg peaks is most clearly seen in the NS-SANS line profiles of Fig. 2, which reveal the appearance and sharpening of peaks at k_h^A and k_h^B with increasing field. The OSR patterns of Fig. 3 exhibit the same evolution of Q_z positions within their respective resolution conditions. A comparison of the Q_z dependence observed in NS-SANS and OSR is shown in Fig. 5. For this comparison, the NS-SANS data were integrated radially within the area enclosed by the red sector shown in Fig. 1(b), and scaled with a single normalization constant for the comparison with all the OSR data. The Q_z dependence of the OSR signal was obtained by integrating the intensity on the negative side of the specular signal for momentum transfers $Q_x \leqslant -3 \times 10^{-6}$ Å^{-1} [see Figs. 3(b) and 3(c)]. All data (Fig. 5) display a single maximum at low [Figs. 5(a1) and 5(b1)] and high fields [Figs. 5(a3) and 5(b3)], respectively, and two maxima at intermediate fields [Figs. 5(a2) and 5(b2)]. Although the measurements have been conducted under very different resolution conditions, and for two different spatial orientations with respect to the in-plane magnetic field, there is very good agreement in the positions of the maxima between the NS-SANS and OSR data.

For the OSR geometry at NREX ($\lambda \approx 4.31$ Å), the off-specular acceptance adjacent to the specular corresponds to in-plane momentum transfers of order $|Q_x| \sim 10^{-3}$ Å^{-1}, i.e., lateral length scales $2\pi/|Q_x| \gtrsim 6 \times 10^3$ Å. By contrast, the NS-SANS geometry used here provides access to in-plane wave vectors up to $|Q_y| \sim 10^{-1}$ Å^{-1}, corresponding to lateral periods down to $\mathcal{O}(10^2)$ Å (see Sec. II within the SM [56] for further details). Thus NS-SANS provides sensitivity to in-plane magnetic modulations at the 100–200 Å scale

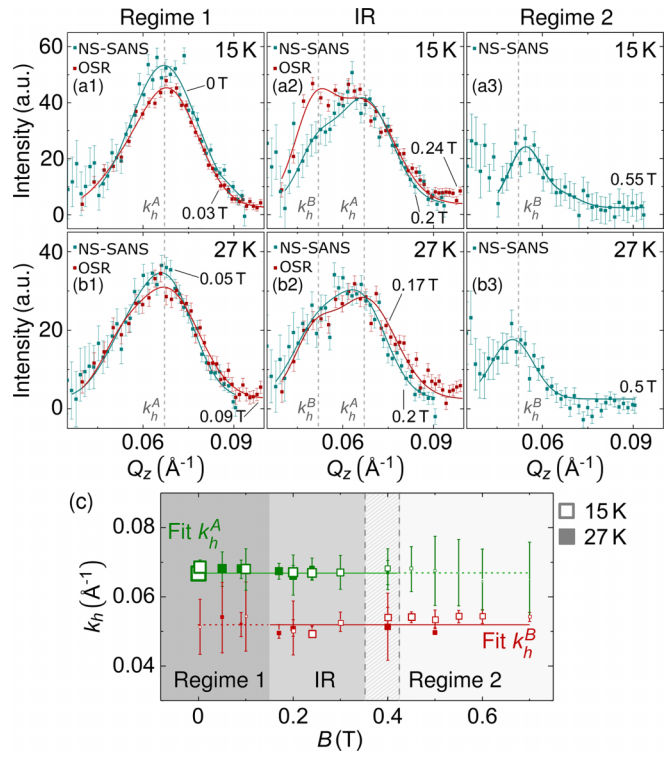


FIG. 5. Comparison of the Q_z dependence observed in NS-SANS and OSR for various fields and temperatures. (a1)–(a3) Field-dependence at 15 K, and (b1)–(b3) at 27 K. The solid lines represent Gaussian fits. (c) Field dependence of the position of the magnetic Bragg peaks A and B. The regimes 1 and 2 are highlighted in dark gray and white, respectively. Dashed vertical lines depict the transition from the intermediate regime (IR) to regime 2.

typical for helical or skyrmion structures, whereas OSR probes only much longer lateral correlations (associated with the film's domain structure). Hence, the primary focus of the OSR measurements was to exploit the measurement's nanoscale Q_z resolution to corroborate the Q_z correlations observed by NS-SANS.

Across all field and temperature regimes and experimental geometries explored, nanoscale-sensitive techniques—namely, NS-SANS probing Q_x, Q_y, and Q_z, and PNR and OSR probing Q_z—reveal that the magnetic signal is periodic only along the Q_z direction, with no scattering at comparable length scales in Q_x or Q_y. This demonstrates that the MnSi film hosts one-dimensional nanoscale magnetic modulations propagating perpendicular to the film surface. From our PNR models, the modulation is likely a helix. Even though the NS-SANS, PNR, and OSR signals cannot be tracked all the way up to T_c and B_c, the accessible temperature and field ranges are sufficiently large to note that we do not find any evidence supporting earlier claims of in-plane skyrmions [23,40].

For fields applied parallel to the film surface, a similar reduction of the helical modulation length under increasing magnetic fields was previously reported in a related study on a 267 Å-thick MnSi film [37,38,42]. Here, PNR data were satisfactorily modeled by a sinusoidal magnetization profile with a wave vector of $Q_z = 0.045$ Å^{-1} in zero field, and a distorted sinusoidal function with a reduced wave vector at increased in-plane magnetic fields of 0.2 T and 0.4 T. The findings of the study were discussed in terms of a field-induced unwinding of a helix in discrete steps [38], with which our data are also consistent, and which agrees with the interplay between the perpendicular magnetic anisotropy, favoring an out-of-plane propagation, and the Zeeman energy under applied fields. It is interesting to note that the magnetic anisotropy constant of our series of epitaxial MnSi films inferred from torque magnetometry is vanishingly small [66] and consistent with estimates based on the magnetization reported in the literature [37]. This result suggests a more subtle origin of the propagation direction other than strain-induced magnetic anisotropies.

We note that an alternative interpretation has been proposed in the literature, in which a high-field Q_z feature is attributed to the Q_z component of in-plane skyrmion strings, while the low-field feature corresponds to an out-of-plane helical modulation [40]. In the present work, this scenario is not supported by the experimental observations. NS-SANS, which provides direct access to in-plane wave vectors at the relevant length scales, shows no finite Q_x or Q_y scattering across all field and temperature regimes as well as scattering geometries studied. In addition, the PNR data are consistently described by depth-dependent magnetization profiles corresponding to modulations along Q_z. Combined, our results indicate that both observed modulations (i.e., k_h^A and k_h^B) arise from helical magnetic structures propagating perpendicular to the film surface. Within the experimental sensitivity and parameter range explored, we therefore find no evidence for in-plane periodic magnetic textures.

IV. DISCUSSION

Combining the neutron scattering data obtained on the epitaxial MnSi film with SQUID magnetometry, the magnetic phase diagram shown in Fig. 6 was constructed. The PNR data (open squares) and NS-SANS/OSR data (closed squares) are fully consistent with each other. The phase boundaries between regime 2 and the field-polarized phase ($B > B_c$), as well as T_c, were inferred from SQUID data. The upper critical field $B_c = 0.93$ T (closed blue circles), as well as $T_c = 42.5$ K (dotted blue vertical line), are significantly higher than the corresponding values in bulk MnSi, and in good agreement with other studies on epitaxial MnSi films in the thick-film limit [23,24,37,72].

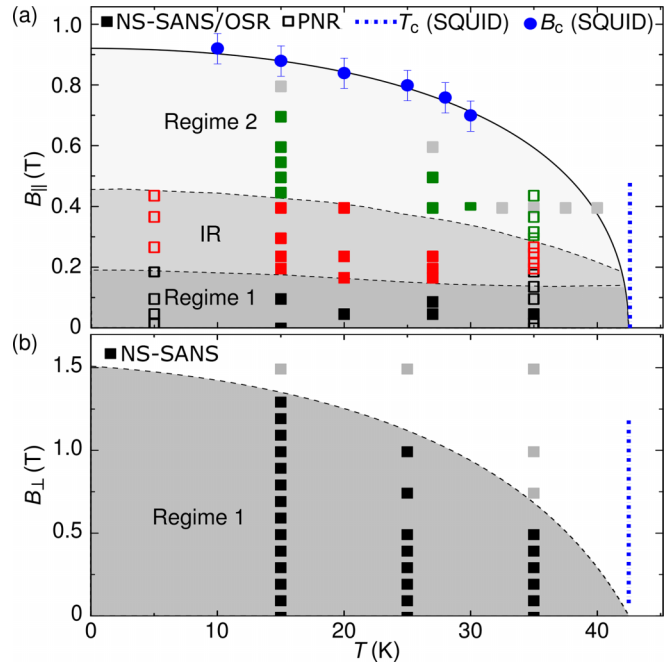


FIG. 6. (B, T)-phase diagrams of the epitaxial MnSi film inferred from NS-SANS, PNR, OSR and SQUID magnetometry. No magnetic signal was observed with NS-SANS at the field and temperature values labeled by gray-shaded squares. (a) Phase diagram under magnetic fields applied parallel to the film surface. Two regimes may be distinguished at low fields and high fields with distinct helical modulations, k_h^A (regime 1) and k_h^B (regime 2), respectively. At intermediate fields both modulations coexist. (b) Phase diagram under magnetic fields applied perpendicular to the film surface. A one-dimensional modulation k_h^A perpendicular to the film surface is observed.

The magnetic order and the phase diagrams we observe bear a striking similarity to the magnetic phase diagram reported for a NS-SANS study on a stack of 32 FeGe films [55]. For epitaxial FeGe, the lattice mismatch is negligibly small, rendering simple strain-induced magnetic anisotropies highly unlikely. For our series of epitaxial MnSi films, EXAFS [65] establishes that lattice strain is released within a few atomic layers of the substrate, indicating that the majority of the film exhibits a relaxed lattice constant consistent with bulk MnSi. EXAFS data additionally reveal small shifts of the Si positions along the [111] direction in the unstrained portion of the film, representing an innate structural difference from bulk MnSi. The shifts of the nonmagnetic atoms give way to an unexpected mechanism that can be responsible for controlling

the magnetic state, leading to the appearance of out-of-plane modulations in epitaxial MnSi in the thick-film limit.

V. CONCLUSIONS

In summary, we present a thorough reciprocal-space mapping of the magnetic order in a single, thick epitaxial MnSi film on Si(111) demonstrating the potential of NS-SANS, PNR, and OSR for identifying helical ordering phenomena. We find a magnetic phase diagram strikingly similar to that of thick epitaxial FeGe. Combining our results with EXAFS and the established properties of thinned bulk samples, we conclude that the magnetic order we observe is consistent with a common out-of-plane helical modulation in thick epitaxial B20 systems studied to date. Our work thus provides a means of unraveling the rather conflicting information on epitaxial B20 films in the literature as concerns the precise mechanisms that allow the tailoring of skyrmions in nanosystems by means of established deposition techniques, although further work is needed to determine the generality of this behavior across other systems and thickness regimes.

ACKNOWLEDGMENTS

We gratefully acknowledge technical support by the team of FRM II as well as Franz Tralmer at NREX. We also wish to thank A. Bauer, M. Brasse, D. Grundler, C. Schnarr, M. Zetzl, and M. Wilde for discussions and support. Financial support through the collaborative research center TRR80 (from Electronic Correlations to Functionality, Project No. 107745057) of the German Research Foundation (DFG) Projects E4 and F7, TRR360 (Constrained Quantum Matter, Project No. 492547816, Projects C1 and C3), SPP2137 (Skyrmionics, Project No. 403191981, Grant No. PF393/19), and the excellence cluster MCQST under Germany's Excellence Strategy EXC-2111 (Project No. 390814868), as well as European Research Council (ERC) Advanced Grant No. 291079 (TOPFIT) and ERC Advanced Grant No. 788031 (ExQuiSid) are gratefully acknowledged. B.W., A.C., M.H., and T.A. acknowledge financial support through the TUM Graduate School. T.H. and S.L.Z. acknowledge the Semiconductor Research Corporation (SRC) under Contract No. 2013- VJ-2394 and EPSRC (UK) under Grant No. EP/N032128/1.

[1] S. Mühlbauer, B. Binz, F. Jonietz, C. Pfleiderer, A. Rosch, A. Neubauer, R. Georgii, and P. Böni, Skyrmion lattice in a chiral magnet, Science **323**, 915 (2009).

[2] A. Neubauer, C. Pfleiderer, B. Binz, A. Rosch, R. Ritz, P. G. Niklowitz, and P. Böni, Topological Hall effect in the *A* phase of MnSi, Phys. Rev. Lett. **102**, 186602 (2009).

[3] W. Münzer, A. Neubauer, T. Adams, S. Mühlbauer, C. Franz, F. Jonietz, R. Georgii, P. Böni, B. Pedersen, M. Schmidt, A. Rosch, and C. Pfleiderer, Skyrmion lattice in the doped semiconductor $Fe_{1-x}Co_xSi$, Phys. Rev. B **81**, 041203(R) (2010).

[4] F. Jonietz, S. Mühlbauer, C. Pfleiderer, A. Neubauer, W. Münzer, A. Bauer, T. Adams, R. Georgii, P. Böni, R. A. Duine, *et al.*, Spin transfer torques in MnSi at ultralow current densities, Science **330**, 1648 (2010).

[5] X. Z. Yu, Y. Onose, N. Kanazawa, J. H. Park, J. H. Han, Y. Matsui, N. Nagaosa, and Y. Tokura, Real-space observation of a two-dimensional skyrmion crystal, Nature (London) **465**, 901 (2010).

[6] X. Z. Yu, N. Kanazawa, Y. Onose, K. Kimoto, W. Z. Zhang, S. Ishiwata, Y. Matsui, and Y. Tokura, Near room-temperature formation of a skyrmion crystal in thin-films of the helimagnet FeGe, Nat. Mater. **10**, 106 (2011).

[7] S. Seki, X. Z. Yu, S. Ishiwata, and Y. Tokura, Observation of skyrmions in a multiferroic material, Science **336**, 198 (2012).

[8] T. Adams, A. Chacon, M. Wagner, A. Bauer, G. Brandl, B. Pedersen, H. Berger, P. Lemmens, and C. Pfleiderer, Long-wavelength helimagnetic order and skyrmion lattice phase in Cu_2OSeO_3, Phys. Rev. Lett. **108**, 237204 (2012).

[9] T. Schulz, R. Ritz, A. Bauer, M. Halder, M. Wagner, C. Franz, C. Pfleiderer, K. Everschor, M. Garst, and A. Rosch, Emergent electrodynamics of skyrmions in a chiral magnet, Nat. Phys. **8**, 301 (2012).

[10] N. Nagaosa and Y. Tokura, Topological properties and dynamics of magnetic skyrmions, Nat. Nanotechnol. **8**, 899 (2013).

[11] P. Milde, D. Köhler, J. Seidel, L. M. Eng, A. Bauer, A. Chacon, J. Kindervater, S. Mühlbauer, C. Pfleiderer, S. Buhrandt, C. Schütte, and A. Rosch, Unwinding of a skyrmion lattice by magnetic monopoles, Science **340**, 1076 (2013).

[12] M. Mochizuki, X. Z. Yu, S. Seki, N. Kanazawa, W. Koshibae, J. Zang, M. Mostovoy, Y. Tokura, and N. Nagaosa, Thermally driven ratchet motion of a skyrmion microcrystal and topological magnon Hall effect, Nat. Mater. **13**, 241 (2014).

[13] T. Schwarze, J. Waizner, M. Garst, A. Bauer, I. Stasinopoulos, H. Berger, C. Pfleiderer, and D. Grundler, Universal helimagnon and skyrmion excitations in metallic, semiconducting and insulating chiral magnets, Nat. Mater. **14**, 478 (2015).

[14] N. S. Kiselev, A. N. Bogdanov, R. Schäfer, and U. K. Rößler, Chiral skyrmions in thin magnetic films: New objects for magnetic storage technologies? J. Phys. D: Appl. Phys. **44**, 392001 (2011).

[15] A. Fert, V. Cros, and J. Sampaio, Skyrmions on the track, Nat. Nanotechnol. **8**, 152 (2013).

[16] F. Hellman, A. Hoffmann, Y. Tserkovnyak, G. S. D. Beach, E. E. Fullerton, C. Leighton, A. H. MacDonald, D. C. Ralph, D. A. Arena, H. A. Dürr, *et al.*, Interface-induced phenomena in magnetism, Rev. Mod. Phys. **89**, 025006 (2017).

[17] M. Garst, J. Waizner, and D. Grundler, Collective spin excitations of helices and magnetic skyrmions: Review and perspectives of magnonics in non-centrosymmetric magnets, J. Phys. D: Appl. Phys. **50**, 293002 (2017).

[18] C. Back, V. Cros, H. Ebert, K. Everschor-Sitte, A. Fert, M. Garst, T. Ma, S. Mankovsky, T. L. Monchesky, M. Mostovoy, *et al.*, The 2020 skyrmionics roadmap, J. Phys. D: Appl. Phys. **53**, 363001 (2020).

[19] Y. Tokura and N. Kanazawa, Magnetic skyrmion materials, Chem. Rev. **121**, 2857 (2021).

[20] A. Tonomura, X. Yu, K. Yanagisawa, T. Matsuda, Y. Onose, N. Kanazawa, H. S. Park, and Y. Tokura, Real-space observation of

skyrmion lattice in helimagnet MnSi thin samples, Nano Lett. **12**, 1673 (2012).

[21] X. Yu, J. P. DeGrave, Y. Hara, T. Hara, S. Jin, and Y. Tokura, Observation of the magnetic skyrmion lattice in a MnSi nanowire by Lorentz TEM, Nano Lett. **13**, 3755 (2013).

[22] E. Karhu, S. Kahwaji, T. L. Monchesky, C. Parsons, M. D. Robertson, and C. Maunders, Structure and magnetic properties of MnSi epitaxial thin films, Phys. Rev. B **82**, 184417 (2010).

[23] M. N. Wilson, E. A. Karhu, A. S. Quigley, U. K. Rößler, A. B. Butenko, A. N. Bogdanov, M. D. Robertson, and T. L. Monchesky, Extended elliptic skyrmion gratings in epitaxial MnSi thin films, Phys. Rev. B **86**, 144420 (2012).

[24] Y. Li, N. Kanazawa, X. Yu, A. Tsukazaki, M. Kawasaki, M. Ichikawa, X. Jin, F. Kagawa, and Y. Tokura, Robust formation of skyrmions and topological Hall effect anomaly in epitaxial thin films of MnSi, Phys. Rev. Lett. **110**, 117202 (2013).

[25] Z. Li, Y. Yuan, R. Hübner, V. Begeza, T. Naumann, L. Rebohle, O. Hellwig, M. Helm, K. Nielsch, S. Prucnal, and S. Zhou, B20-MnSi films grown on Si(100) substrates with magnetic skyrmion signature, Mater. Today Phys. **21**, 100541 (2021).

[26] Z. Li, Y. Xie, Y. Yuan, Y. Ji, V. Begeza, L. Cao, R. Hübner, L. Rebohle, M. Helm, K. Nielsch, S. Prucnal, and S. Zhou, Phase selection in Mn-Si alloys by fast solid-state reaction with enhanced skyrmion stability, Adv. Funct. Mater. **31**, 2009723 (2021).

[27] T. Yokouchi, N. Kanazawa, A. Tsukazaki, Y. Kozuka, M. Kawasaki, M. Ichikawa, F. Kagawa, and Y. Tokura, Stability of two-dimensional skyrmions in thin films of $Mn_{1-x}Fe_xSi$ investigated by the topological Hall effect, Phys. Rev. B **89**, 064416 (2014).

[28] N. A. Porter, P. Sinha, M. B. Ward, A. N. Dobrynin, R. M. D. Brydson, T. R. Charlton, C. J. Kinane, M. D. Robertson, S. Langridge, and C. H. Marrows, Giant topological Hall effect in strained $Fe_{0.7}Co_{0.3}Si$ epilayers, arXiv:1312.1722.

[29] P. Sinha, N. A. Porter, and C. H. Marrows, Strain-induced effects on the magnetic and electronic properties of epitaxial $Fe_{1-x}Co_xSi$ thin films, Phys. Rev. B **89**, 134426 (2014).

[30] N. A. Porter, J. C. Gartside, and C. H. Marrows, Scattering mechanisms in textured FeGe thin films: Magnetoresistance and the anomalous Hall effect, Phys. Rev. B **90**, 024403 (2014).

[31] J. C. Gallagher, K. Y. Meng, J. T. Brangham, H. L. Wang, B. D. Esser, D. W. McComb, and F. Y. Yang, Robust zero-field skyrmion formation in FeGe epitaxial thin films, Phys. Rev. Lett. **118**, 027201 (2017).

[32] A. S. Ahmed, J. Rowland, B. D. Esser, S. R. Dunsiger, D. W. McComb, M. Randeria, and R. K. Kawakami, Chiral bobbers and skyrmions in epitaxial FeGe/Si(111) films, Phys. Rev. Mater. **2**, 041401(R) (2018).

[33] K.-Y. Meng, A. S. Ahmed, M. Bacáni, A.-O. Mandru, X. Zhao, N. Bagueś, B. D. Esser, J. Flores, D. W. McComb, H. J. Hug, and F. Yang, Observation of nanoscale skyrmions in $SrIrO_3/SrRuO_3$ bilayers, Nano Lett. **19**, 3169 (2019).

[34] T. L. Monchesky, J. C. Loudon, M. D. Robertson, and A. N. Bogdanov, Comment on "Robust formation of skyrmions and topological Hall effect anomaly in epitaxial thin films of MnSi", Phys. Rev. Lett. **112**, 059701 (2014).

[35] Y. Li, N. Kanazawa, X. Z. Yu, F. Kagawa, and Y. Tokura, Li *et al.* Reply, Phys. Rev. Lett. **112**, 059702 (2014).

[36] S. A. Meynell, M. N. Wilson, J. C. Loudon, A. Spitzig, F. N. Rybakov, M. B. Johnson, and T. L. Monchesky, Hall effect and transmission electron microscopy of epitaxial MnSi thin films, Phys. Rev. B **90**, 224419 (2014).

[37] E. A. Karhu, U. K. Rößler, A. N. Bogdanov, S. Kahwaji, B. J. Kirby, H. Fritzsche, M. D. Robertson, C. F. Majkrzak, and T. L. Monchesky, Chiral modulations and reorientation effects in MnSi thin films, Phys. Rev. B **85**, 094429 (2012).

[38] M. N. Wilson, E. A. Karhu, D. P. Lake, A. S. Quigley, S. Meynell, A. N. Bogdanov, H. Fritzsche, U. K. Rößler, and T. L. Monchesky, Discrete helicoidal states in chiral magnetic thin films, Phys. Rev. B **88**, 214420 (2013).

[39] T. Yokouchi, N. Kanazawa, A. Tsukazaki, Y. Kozuka, A. Kikkawa, Y. Taguchi, M. Kawasaki, M. Ichikawa, F. Kagawa, and Y. Tokura, Formation of in-plane skyrmions in epitaxial MnSi thin films as revealed by planar Hall effect, J. Phys. Soc. Jpn. **84**, 104708 (2015).

[40] S. A. Meynell, M. N. Wilson, K. L. Krycka, B. J. Kirby, H. Fritzsche, and T. L. Monchesky, Neutron study of in-plane skyrmions in MnSi thin films, Phys. Rev. B **96**, 054402 (2017).

[41] E. A. Karhu, S. Kahwaji, M. D. Robertson, H. Fritzsche, B. J. Kirby, C. F. Majkrzak, and T. L. Monchesky, Helical magnetic order in MnSi thin films, Phys. Rev. B **84**, 060404(R) (2011).

[42] M. N. Wilson, A. B. Butenko, A. N. Bogdanov, and T. L. Monchesky, Chiral skyrmions in cubic helimagnet films: The role of uniaxial anisotropy, Phys. Rev. B **89**, 094411 (2014).

[43] S. A. Meynell, M. N. Wilson, H. Fritzsche, A. N. Bogdanov, and T. L. Monchesky, Surface twist instabilities and skyrmion states in chiral ferromagnets, Phys. Rev. B **90**, 014406 (2014).

[44] G. L. Causer, L. Guasco, O. Paull, and D. Cortie, Topical review of quantum materials and heterostructures studied by polarized neutron reflectometry, Phys. Status Solidi RRL **17**, 2200421 (2023).

[45] J. H. Han, J. Zang, Z. Yang, J.-H. Park, and N. Nagaosa, Skyrmion lattice in a two-dimensional chiral magnet, Phys. Rev. B **82**, 094429 (2010).

[46] F. N. Rybakov, A. B. Borisov, S. Blügel, and N. S. Kiselev, New type of stable particlelike states in chiral magnets, Phys. Rev. Lett. **115**, 117201 (2015).

[47] F. Zheng, F. N. Rybakov, A. B. Borisov, D. Song, S. Wang, Z.-A. Li, H. Du, N. S. Kiselev, J. Caron, A. Kovács, *et al.*, Experimental observation of chiral magnetic bobbers in B20-type FeGe, Nat. Nanotechnol. **13**, 451 (2018).

[48] J. Wild, T. N. G. Meier, S. Pöllath, M. Kronseder, A. Bauer, A. Chacon, M. Halder, M. Schowalter, A. Rosenauer, J. Zweck, *et al.*, Entropy-limited topological protection of skyrmions, Sci. Adv. **3**, e1701704 (2017).

[49] S. Heinze, K. von Bergmann, M. Menzel, J. Brede, A. Kubetzka, R. Wiesendanger, G. Bihlmayer, and S. Blügel, Spontaneous atomic-scale magnetic skyrmion lattice in two dimensions, Nat. Phys. **7**, 713 (2011).

[50] N. Romming, C. Hanneken, M. Menzel, J. E. Bickel, B. Wolter, K. von Bergmann, A. Kubetzka, and R. Wiesendanger, Writing and deleting single magnetic skyrmions, Science **341**, 636 (2013).

[51] A. B. Butenko, A. A. Leonov, U. K. Rößler, and A. N. Bogdanov, Stabilization of skyrmion textures by uniaxial distortions in noncentrosymmetric cubic helimagnets, Phys. Rev. B **82**, 052403 (2010).

[52] A. A. Leonov, A. N. Bogdanov, and U. K. Roessler, Confinement of skyrmion states in noncentrosymmetric magnets, arXiv:1001.1292.

[53] U. K. Rößler, A. A. Leonov, and A. N. Bogdanov, Chiral skyrmionic matter in non-centrosymmetric magnets, J. Phys.: Conf. Ser. **303**, 012105 (2011).

[54] F. N. Rybakov, A. B. Borisov, and A. N. Bogdanov, Three-dimensional skyrmion states in thin films of cubic helimagnets, Phys. Rev. B **87**, 094424 (2013).

[55] N. Kanazawa, J. S. White, H. M. Rønnow, C. D. Dewhurst, Y. Fujishiro, A. Tsukazaki, Y. Kozuka, M. Kawasaki, M. Ichikawa, F. Kagawa, and Y. Tokura, Direct observation of anisotropic magnetic field response of the spin helix in FeGe thin films, Phys. Rev. B **94**, 184432 (2016).

[56] See Supplemental Material at http://link.aps.org/supplemental/10.1103/pss4-vlyr for calculated scattering patterns, experimental methods, and further experimental results.

[57] D. Schroeter, N. Steinki, M. Schilling, A. Fernández Scarioni, P. Krzysteczko, T. Dziomba, H. W. Schumacher, D. Menzel, and S. Süllow, MnSi nanostructures obtained from epitaxially grown thin films: Magnetotransport and Hall effect, J. Phys.: Condens. Matter **30**, 235805 (2018).

[58] J. Engelke, T. Reimann, L. Hoffmann, S. Gass, D. Menzel, and S. Süllow, Spin–spin correlation length in MnSi thin films, J. Phys. Soc. Jpn. **81**, 124709 (2012).

[59] D. Bloch, J. Voiron, V. Jaccarino, and J. H. Wernick, High field high pressure magnetic-properties of MnSi, Phys. Lett. A **51**, 259 (1975).

[60] M. Lee, Y. Onose, Y. Tokura, and N. P. Ong, Hidden constant in the anomalous Hall effect of high-purity magnet MnSi, Phys. Rev. B **75**, 172403 (2007).

[61] L. G. Parratt, Surface studies of solids by total reflection of x-rays, Phys. Rev. **95**, 359 (1954).

[62] G. L. Causer, A. Chacon, A. Heinemann, and C. Pfleiderer, Small-angle neutron scattering of long-wavelength magnetic modulations in reduced sample dimensions, J. Appl. Crystallogr. **56**, 26 (2023).

[63] G. L. Causer, Opportunities for near-surface small-angle neutron scattering to probe magnetic nanostructures within thin-film volumes, J. Appl. Crystallogr. **58**, 1455 (2025).

[64] B. Wiedemann, Magnetic and structural properties of Fe and MnSi thin films investigated by scattering techniques, Ph.D. thesis, Technical University of Munich, 2014.

[65] A. I. Figueroa, S. L. Zhang, A. A. Baker, R. Chalasani, A. Kohn, S. C. Speller, D. Gianolio, C. Pfleiderer, G. van der Laan, and T. Hesjedal, Strain in epitaxial MnSi films on Si(111) in the thick film limit studied by polarization-dependent extended x-ray absorption fine structure, Phys. Rev. B **94**, 174107 (2016).

[66] M. Brasse, Magnetization of correlated electron systems: MnSi thin films, CrB_2 single crystals and two-dimensional electron systems in MgZnO/ZnO, Ph.D. thesis, Technical University of Munich, 2013.

[67] D. Menzel, J. Engelke, T. Reimann, and S. Süllow, Enhanced critical fields in MnSi thin films, J. Korean Phys. Soc. **62**, 1580 (2013).

[68] T. Lancaster, F. Xiao, Z. Salman, I. O. Thomas, S. J. Blundell, F. L. Pratt, S. J. Clark, T. Prokscha, A. Suter, S. L. Zhang, A. A. Baker, and T. Hesjedal, Transverse field muon-spin rotation measurement of the topological anomaly in a thin film of MnSi, Phys. Rev. B **93**, 140412(R) (2016).

[69] S. L. Zhang, R. Chalasani, A. A. Baker, N.-J. Steinke, A. I. Figueroa, A. Kohn, G. van der Laan, and T. Hesjedal, Engineering helimagnetism in MnSi thin films, AIP Adv. **6**, 015217 (2016).

[70] S. Mühlbauer, A. Heinemann, A. Wilhelm, L. Karge, A. Ostermann, I. Defendi, A. Schreyer, W. Petry, and R. Gilles, The new small-angle neutron scattering instrument SANS-1 at MLZ—characterization and first results, Nucl. Instrum. Methods Phys. Res. A: Accel. Spectrom. Detect. Assoc. Equip **832**, 297 (2016).

[71] Y. Khaydukov, O. Soltwedel, and T. Keller, NREX: Neutron reflectometer with x-ray option, JLSRF **1**, A38 (2015).

[72] Z. Li, Y. Yuan, V. Begeza, L. Rebohle, M. Helm, K. Nielsch, S. Prucnal, and S. Zhou, On Curie temperature of B20-MnSi films, Sci. Rep. **12**, 16388 (2022).